mathematics

Article

Application and CFD-Based Optimization of a Novel Porous Object for Confined Slot Jet Impingement Cooling Systems under a Magnetic Field

Walid Aich [1], Fatih Selimefendigil [2,*], Badreddine Ayadi [1,3], Lotfi Ben Said [1], Badr M. Alshammari [4], Lioua Kolsi [1,5], Sid Ali Betrouni [1] and Hatem Gasmi [6]

1 Department of Mechanical Engineering, College of Engineering, University of Ha'il, Ha'il City 81451, Saudi Arabia; w.aich@uoh.edu.sa (W.A.); b.ayadi@uoh.edu.sa (B.A.); bensaid_rmq@yahoo.fr (L.B.S.); l.kolsi@uoh.edu.sa (L.K.); s.betrouni@uoh.edu.sa (S.A.B.)
2 Department of Mechanical Engineering, Celal Bayar University, 45140 Manisa, Turkey
3 Laboratory of Applied Fluid Mechanics, Environment and Process Engineering "LR11ES57", National School of Engineers of Sfax (ENIS), University of Sfax, Route Soukra Km 3.5, Sfax 3038, Tunisia
4 Department of Electrical Engineering, College of Engineering, University of Ha'il, Ha'il City 81451, Saudi Arabia; bms.alshammari@uoh.edu.sa
5 Laboratory of Metrology and Energy Systems, Energy Engineering Department, National Engineering School, University of Monastir, Monastir 5000, Tunisia
6 Department of Civil Engineering, College of Engineering, University of Ha'il, Ha'il City 81451, Saudi Arabia; h.gasmi@uoh.edu.sa
* Correspondence: fatih.selimefendigil@cbu.edu.tr; Tel.: +90-236-241-21-44; Fax: +90-236-241-21-43

check for updates

Citation: Aich, W.; Selimefendigil, F.; Ayadi, B.; Ben Said, L.; Alshammari, B.M.; Kolsi, L.; Betrouni, S.A.; Gasmi, H. Application and CFD-Based Optimization of a Novel Porous Object for Confined Slot Jet Impingement Cooling Systems under a Magnetic Field. *Mathematics* **2022**, *10*, 2578. https://doi.org/10.3390/math10152578

Academic Editor: James M. Buick

Received: 17 June 2022
Accepted: 19 July 2022
Published: 25 July 2022

Abstract: A novel porous object for the control of the convective heat transfer of confined slot nanojet impingement is offered under magnetic field effects, while optimization-assisted computational fluid dynamics is used to find the best working conditions to achieve the best performance of the system. The flow, thermal patterns, and heat transfer characteristics were influenced by the variation in rotational Reynolds number (Rew), Hartmann number (Ha), permeability of the porous object (Da) and its location (Mx). There was a 14.5% difference in the average Nusselt number (Nu) at the highest Rew when motionless object configuration at Ha = 5 was compared, while it was less than 2% at Ha = 25. At Rew = −600, the average Nu variation was 22% when cases with the lowest and highest magnetic field strength were compared. The porous object provides an excellent tool for convective heat transfer control, while the best performance was achieved by using optimization-assisted computational fluid dynamics. The optimal sets of (Rew, Da, Mx, AR) for porous object were (−315.97, 0.0188, −1.456, 0.235), (−181.167, 0.0167, −1.441, 0.2), and (−483.13, 0.0210, −0.348, 0.2) at Ha = 5, 10, and 25, respectively. At the optimal operating point, the local Nu enhancements were 19.46%, 44.86%, and −0.54% at Ha = 5, 10, and 15, respectively, when the no-object case was compared, while the average values were 7.87%, 8.09% and 5.04%.

Keywords: jet impingement; optimization; MHD; hybrid nanofluid; finite element method; COBYLA

MSC: 76D25; 76D55; 80M10; 80M50; 76S05

1. Introduction

Heat-transfer (HT) applications with impinging jets can be encountered in various applications, such as in solar energy, drying, chemical processes, microelectromechanical systems (MEMS), glass tempering, and the food and agricultural industry. The interaction among the established recirculation zone (RZ), pressure gradients, and thermal field within a complex geometry complicates the process to treat the problem analytically. Many different geometric factors and operating parameters play a role in the performance of convective HT with impinging jets. Jambunathan et al. [1] reviewed experimental data for impinging jets in turbulent regime for the range of Reynolds numbers between 5000 and 124,000, while a single circular jet was considered at different nozzle plate distances. The available correlation for the Nusselt number was improved. Krishan et al. [2] presented a review for the applications of synthetic jet which was considered as a novel thermal management method. Different parametric effects such as the optimal distance between the jet and target surface, jet number, and frequency of excitation on the performance enhancements were explored along with future challenges and gaps. The effectiveness of impinging jets can be improved by using different passive and active HT enhancement techniques. Flow pulsations are a control method by adjusting the frequency and amplitude of pulsating flow [3–5]. The curvature [6,7] and elasticity [8] effects of the surfaces were also addressed for jet impingement HT configurations, and they were influential on convective cooling performance. The porosity of the medium is also taken into consideration for jet impingement HT applications [9–11].

The installation of stationary, moving, and rotating objects of different shapes was considered in the thermal management of diverse energy systems. The impacts of using rotations on fluid-flow convective HT characteristics were considered in many thermofluid systems [12,13]. In the work of Yacob et al. [14], steady 3D rotating flow past a stretching or shrinking surface was analyzed with water and nanofluid, and the increment of the rotating flow parameter resulted in a reduction in HT. When rotating cylinders are used in convective HT applications, the size, rotational speed, and location of the cylinders are the main parameters that influence the fluid flow and HT performance features [15–17]. The effectiveness of jet impingement HT can be increased by using those techniques. Wang et al. [18] performed experimental work for controlling the HT for jet impingement in cross-flow by using a rib. They used the LCT technique, and significant variations and enhancements in the HT were achieved with the presence of the rib in the system. Iwana et al. [19] proposed a novel device for flow control in jet impingement HT. The device included triangular tabs. When the system was operated with a combined device, up to a 35% increase in peak local Nusselt number was achieved. Selimefendigil and Öztop [20] analyzed the slot jet impingement (SJ-I) HT while using a rotating cylinder. At the highest rotational speed, the average Nu variations of 20.16% were achieved for the SJ-I system. Nagesha et al. [21] performed experimental analysis for jet impingement HT by using roughness elements. Different elements such as multiprotrusions and V grooves wee used; by using well-separated protrusions, higher heat transfer was achieved than that in the case with V grooves that were closely spaced.

In HT, magnetic field (MaF) effects are used for flow and HT control. Magnetohydrodynamics (MHD), which considers the interaction between the MaF and electrically conducting fluid, has been used in diverse technological applications such as in processes of continuous casting, cooling in the nuclear industry, lubrication, microfluidic devices, and drug delivery in medical and many other systems. The effectiveness and potential applications of MaF can be further increased by utilizing nanoparticles in HT fluid. Many aspects of MaF, including utilization with nanofluids, were considered in diverse thermal engineering systems [22–24]. MaF effects with rotations were also considered in several works [25,26]. Oke [27] studied modified Eyring–Powell fluid flow over a rotating and stretching surface considering the combined impacts of thermal radiation and magnetic field. The Coriolis force reduced the primary velocity, but the temperature profile was enhanced. The velocity was reduced with a magnetic field, while the temperature profile was increased. In the work of Selimefendigil and Öztop [28], flow separation and hydrothermal performance features in a channel with area expansion were affected by the rotation, arrangement, and locations of the cylinders in the channel. HT performance was enhanced with higher MaF strengths. M'hamed et al. [29] presented a review on applications of MaF on nanofluids with many industrial examples. As the major challenges in commercialization, stability and cost issues were mentioned. In another review, various HT applications of nanofluids with the presence of MaF effects were analyzed Sheikholeslami and Rokni [30]. Different numerical and experimental results were provided considering single- and two-phase approaches of nanofluids with MaF. Many studies showed the effectiveness of using nanofluids in jet impinging systems [31–33]. Depending upon the nanoparticle loading amount, particle type, and jet flow system configuration, different enhancements were reported. Mohammadpour and Lee [34] presented an extensive review of the nanofluid applications of jet impingement HT. Non-Newtonian aspects of fluid, and single- and two-phase models of nanofluid were considered. A single-phase non-Newtonian model gave higher HT coefficients, while more pumping power was needed as compared to Newtonian fluid. HT efficiency may have also been affected by nanoparticle deposition. In a recent review, Tyagi et al. [35] studied the applications of spray or jet impingement cooling with nanofluids. The essential features of cooling performance for the jet or spray cooling along with the nanofluid properties were discussed. The applications of MaF were considered in a few studies for impinging jet HT [36] and with nanofluids [37,38].

In the present study, a novel porous object (NPO) is used for the convective HT control and thermal management of the slot jet impingement (SJ-I) cooling systems of nanofluids under MaF effects. The object was an annular porous cylinder of which the inner surface was rotating. In the literature, the application of MaF for SJ-I cooling has been considered in many studies, as mentioned above. However, the utilization of such a novel device under MaF effects has never been considered. Cooling performance improvement is achieved by using the NPO and varying its operating parameters. Different aspect ratios and permeabilities can be assigned to the NPO, while its location can also be varied within a SJ-I cooling system. Computational fluid dynamics (CFD) simulations are performed to find the impacts of different operating and geometric parameters of interest. However, a parametric variation of the NPO geometric factors may not give the best working conditions of the device for different operating points (MaF strength). Therefore, an optimization algorithm is used to assist the CFD simulations to achieve the optimal parameters of interest and achieve the highest cooling rate. The outcomes of the present work are helpful in the design and development of cooling systems with impinging jets that can be utilized in the thermal management of diverse energy system technologies.

2. Mathematical Model

The impacts of using a novel porous object and MaF on confined slot jet impingement (SJ-I) cooling performance are explored. A schematic view of the configuration is shown in Figure 1. The novel object was a porous circular cylinder, and its inner part rotated at speed Ω. Its center was located at position (xr, yr); the radii of the inner and outer parts are denoted as R1 and R2. The aspect ratio was defined as AR = R2/R1. The confined SJ-I system had a slot with WD, and its distance to the hot isothermal surface was H. The length of the plate was L; cold fluid with velocity ug and temperature Tg impinged onto the hot plate with temperature Th. An external MaF was imposed with strength $\vec{B}$ and inclination γ. As the HT fluid, a hybrid nanofluid with water containing Ag–MgO hybrid nanoparticles was used. The nanofluid viscosity and thermal conductivity were obtained from the experimental data, and correlations by using these data were considered in the numerical model. A singe-phase nanofluid modeling approach was considered for the solid volume fraction of 0.02. When external MaF effects are taken into account, effects such as Joule heating, displacement currents, and induced MaF are ignored, while natural convection, radiation, and viscous dissipation effects were not considered. In the domain of the NPO, the generalized Darcy–Brinkmann Forchheimer extended porous model was considered.

The conservation equations in the SJ-I domain except for the porous region are given below [39]:

$$\frac{\partial u}{\partial x} + \frac{\partial v}{\partial y} = 0, \tag{1}$$

$$u\frac{\partial u}{\partial x} + v\frac{\partial u}{\partial y} = -\frac{1}{\rho_{nf}}\frac{\partial p}{\partial x} + \nu_{nf}\left(\frac{\partial^2 u}{\partial x^2} + \frac{\partial^2 u}{\partial y^2}\right) + \frac{\sigma_{nf}B^2}{\rho_{nf}}\left(v\cos\gamma\sin\gamma - u\sin^2\gamma\right), \tag{2}$$

$$u\frac{\partial v}{\partial x}+v\frac{\partial v}{\partial y}=-\frac{1}{\rho_{nf}}\frac{\partial p}{\partial y}+\nu_{nf}\left(\frac{\partial^2 v}{\partial x^2}+\frac{\partial^2 v}{\partial y^2}\right)+\frac{\sigma_{nf}B^2}{\rho_{nf}}\left(u\cos\gamma\sin\gamma-v\cos^2\gamma\right), \tag{3}$$

$$u\frac{\partial T}{\partial x}+v\frac{\partial T}{\partial y}=\alpha_{nf}\left(\frac{\partial^2 T}{\partial x^2}+\frac{\partial^2 T}{\partial y^2}\right), \tag{4}$$

where B and γ are the strength and inclination angle of the MaF, respectively.

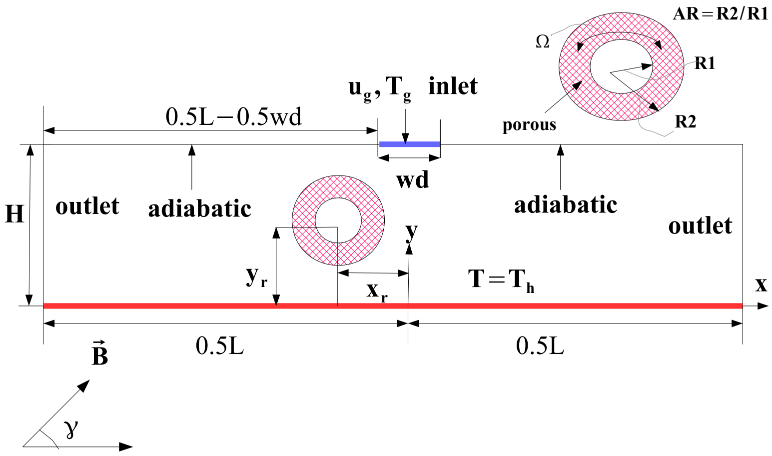

Figure 1. Model description with boundary conditions.

In the NPO domain, they are given as follows [39,40]:

$$\frac{\partial u}{\partial x}+\frac{\partial v}{\partial y}=0, \tag{5}$$

$$\begin{aligned}\frac{1}{\varepsilon^2}\left(u\frac{\partial u}{\partial x}+v\frac{\partial u}{\partial y}\right)&=-\frac{1}{\rho_{nf}}\frac{\partial p}{\partial x}+\frac{\nu_{nf}}{\varepsilon}\left(\nabla^2 u\right)\\&-\nu_{nf}\frac{u}{K}-\frac{F_c}{\sqrt{K}}u\sqrt{u^2+v^2}+\frac{\sigma_{nf}B^2}{\rho_{nf}}\left(v\sin(\gamma)\cos(\gamma)-u\sin^2\gamma\right),\end{aligned} \tag{6}$$

$$\begin{aligned}\frac{1}{\varepsilon^2}\left(u\frac{\partial v}{\partial x}+v\frac{\partial v}{\partial y}\right)&=-\frac{1}{\rho_{nf}}\frac{\partial p}{\partial y}+\frac{\nu_{nf}}{\varepsilon}\left(\nabla^2 v\right)\\&-\nu_{nf}\frac{v}{K}-\frac{F_c}{\sqrt{K}}v\sqrt{u^2+v^2}+\frac{\sigma_{nf}B^2}{\rho_{nf}}\left(u\sin(\gamma)\cos(\gamma)-v\cos^2\gamma\right),\end{aligned} \tag{7}$$

$$u\frac{\partial T}{\partial x}+v\frac{\partial T}{\partial y}=\alpha\nabla^2 T. \tag{8}$$

In the above equations, the generalized Darcy–Brinkmann Forchheimer extended porous model was used. The last terms on the right-hand side of the momentum equations include the Lorentz forces due to the external MaF; under the simplified assumptions of magnetic field effects, the above-given simplified forms are obtained [39,40].

In dimensional form, the boundary conditions can be stated as in the following:

- Jet inlet,
  $u=0,\ v=u_g,\ T=T_g.$
- SJ-I exit:
  $\frac{\partial u}{\partial x}=0,\ \frac{\partial v}{\partial x}=0,\ \frac{\partial T}{\partial x}=0.$
- Adiabatic top plate:
  $u=v=0,\ \frac{\partial T}{\partial y}=0.$
- At the interface between nanofluid and porous domain:
  $u_f=u_p,\ v_f=v_p,\ k_f\left(\frac{\partial T}{\partial x}\right)_f=k_p\left(\frac{\partial T}{\partial x}\right)_p.$

- On the rotating inner surface of the NPO:
  $u = -\omega(y - y_r),\ \ v = \omega(x - x_r),\ \ \frac{\partial T}{\partial n} = 0.$
  The relevant physical nondimensional parameters of interest are:

$$\mathrm{Re} = \frac{\rho u_g D_h}{\mu},\ \ \mathrm{Rew} = \frac{\rho(\omega D_h)D_h}{\mu},\ \ \mathrm{Pr} = \frac{\nu}{\alpha},\ \ \mathrm{Ha} = BD_h\sqrt{\frac{\sigma}{\mu}}, \tag{9}$$

where Re, Rew, Pr and Ha are the Reynolds number, rotational Reynolds number, Prandtl number, and Hartmann number, respectively. D_h is the characteristic length that is given by $D_h = 2wd$ for slot width wd. The impacts of the rotation of the inner part of the NPO on the HT characteristics are indicated by the rotational Reynolds number (Rew).

The equations were solved by using a Galerkin weighted residual FEM. Lagrangian FEMs of different orders were used for the approximation of flow-field variables (Vr) as follows:

$$Vr = \sum_{k=1}^{N^s} \Phi_k^s F_k, \tag{10}$$

where Φ^s and F denote the shape function and nodal value, respectively. The weight average of residuals R is expressed as follows:

$$\int_V WRdV = 0, \tag{11}$$

where W is the weight function. The streamline upwind Petrov–Galerkin (SUPG) method was utilized in the solver to handle the local numerical instabilities, while the Biconjugate Gradient Stabilized (BICGStab) solver was used for the fluid flow and heat transfer code modules. A converge criterion of 10^{-7} was selected to achieve the converged solutions. Local (Nu_s) and average Nu (Nu_m) were used for the cooling performance of the SJ-I system with NPO:

$$\mathrm{Nu}_s = \frac{h_s D_h}{k_{nf}} = -\frac{D_h}{T_h - T_c}\frac{\partial T}{\partial s}_w,\ \ \mathrm{Nu}_m = \frac{1}{L}\int_0^L \mathrm{Nu}_s ds, \tag{12}$$

where h_s and L are the local heat transfer coefficient and hot plate length, respectively.

3. Optimization Method

An optimization algorithm was used to find the best operating conditions to achieve the best cooling performance for the NPO considering different MaF strength levels.

In the present study, when the SJ-I system was parametrized, control variables were used. A function of the PDE solution was achieved, namely, the average Nu in PDE constraint optimization. In the general optimization, the PDE problem was considered to be an equality constraint as in the following [41,42]:

$$\begin{aligned} \underset{\psi}{\text{minimize}} \quad & \mathrm{f}(\Phi(\psi), \psi), \\ \text{subject to} \quad & \zeta(\Phi(\psi), \psi) = 0, \\ & lb \le G(\Phi(\psi), \psi) \le ub, \end{aligned} \tag{13}$$

where ψ and Φ are the control variables and PDE solutions, while G represents the constraints. In the current study, the Constrained Optimization BY Linear Approximations (COBYLA) optimization routine, which is a gradient-free technique, was used. Interpolation at the vertices of a simplex was conducted; at each iteration step, it was performed inside a trust region. The rotational speed (Rew), permeability (Da), aspect ratio (AR) and horizontal location(Mx) of the NPO were examined via an optimization method to achieve the highest cooling performance the SJ-I system. Then, the lower (lb) and upper bounds (ub) for the parameters of interest were considered:

$$-600 \le \mathrm{Rew} \le 600,\ \ 10^{-5} \le \mathrm{Da} \le 0.1,\ \ -2 \le \mathrm{Mx} \le 2,\ \ 0.8 \le \mathrm{AR} \le 0.2. \tag{14}$$

We searched for the optimal set of parameters by using COBYLA for three different MaF strengths at Ha = 5, 10, and 15, while the value of Re was kept constant at Re = 300.

4. Grid Independence and Code Validation

Grid independence tests of the solution were performed. The test results at two different MaF strengths are shown in Figure 2a with different grid sizes. The grid with GR-4 was considered that consisted of 262,223 elements. Grid refinement was conducted near the interfaces and toward the walls, as shown in Figure 2b.

The numerical code was validated by using different studies available in the literature. In the first study, the results of [43] for the MaF effects on convective HT are used. Convection in a cavity with MaF effects was analyzed in Ref. [43]. Figure 3 presents the comparison results of the average Nu considering different MaF strengths at Gr = 2 $\times$ 10^4. The maximal difference between the results was 4.10% at Ha = 10. In the second validation study, the numerical results of [44] were used, where an SJ-I system for an isothermal surface was analyzed. Figure 4 presents the local variation in Nu along the bottom wall at Re = 250. The final validation was performed by using the available results in [45,46] where the confined SJ-I cooling performance was analyzed. Table 1 shows the comparison results for stagnation point Nu at Re = 300. A maximal difference of 1.55% was observed between the results. The comparison results show that the present code is capable of simulating SJ-I HT and convective HT with MaF effects.

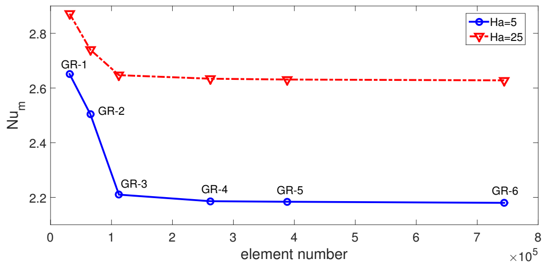

(**a**)

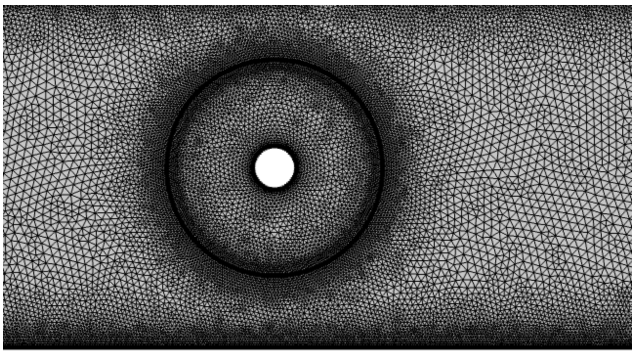

(**b**)

Figure 2. Grid independence test. Average Nu for different grid sizes at two different MaF strength levels (**a**) and mesh distribution of the SJ-I with NPO (**b**) (Rew = -600, Da $= 5 \times 10^{-2}$, Mx = -1, AR = 0.5).

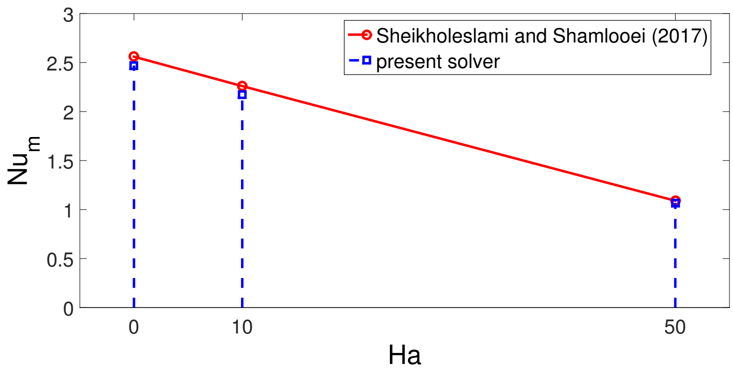

Figure 3. Code validation 1: average Nusselt number comparison with the results of [43] for different Hartmann numbers.

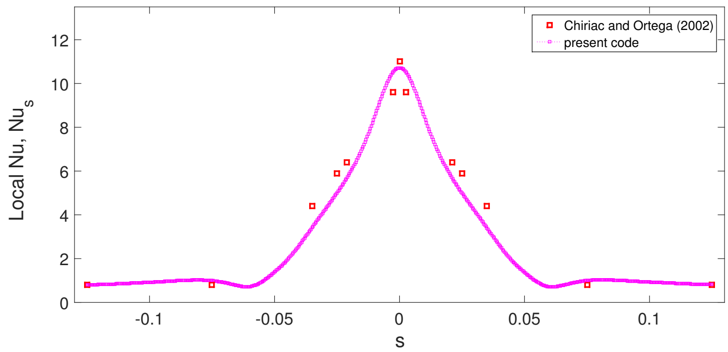

Figure 4. Code validation 2: comparison results of local Nu at Reynolds number of 250 with those in [44].

Table 1. Code validation 3: comparisons of stagnation point Nu at Reynolds number of 300.

Study	Stagnation Nu
This code	9.81
In [46]	9.66
In [45]	9.85

5. Results and Discussion

In the present work, the cooling performance of an SJ–I system using a novel porous object (NPO) under MaF effects was numerically assessed. The NPO was a porous hollow circular cylinder with an inner rotating surface. In the first part of the numerical work, the trends in the variations of local and average Nu with varying parameters of interest were analyzed; the rotational Re number ($-600 \leq$ Rew ≤ 600), Darcy number ($10^{-5} \leq$ Da ≤ 0.1), horizontal location of the NPO ($-2 \leq$ Mx ≤ 2), and aspect ratio ($0.8 \leq$ AR ≤ 0.2) were considered. MaF strength was considered for Hartmann numbers (Ha) between 5 and 25. The COBYLA optimization algorithm was used to find the optimal set of parameters (Rew, Da, Mx, AR) at three different MaF strengths of Ha = 5, Ha = 10, and Ha = 25.

The impacts of the rotational Reynolds number (Rew) on the streamline variation are shown in Figure 5 at two different MaF strength levels. The configuration without NPO is also included. Due to confinement and entertainment, large vortices were seen near the jet inlet, while a small vortex was established on the bottom wall at Ha = 5 when no object was installed. However, as the strength of MaF increased, suppression of the vortices was observed, and the jet impinged onto the hot surface with an inclination for the case without object. The presence of the NPO and its rotation impacted the flow field variations. When the NPO was stationary (Rew = 0), at Ha = 5, the vortex near the left part of the inlet jet shrank, while at Ha = 25, the vortices and the main jet stream near the inlet were elongated toward the left. When the object was rotated clockwise (CW) at the highest speed, the main jet stream was directed toward the right part, while vortices were established in the right part of the rotation NPO. The counter-CW rotation of the object directed the main jet toward the left, and a large recirculation near the object was formed. As the MaF strength increased, the vortices were suppressed, and the dominance of the rotating object's effects on the flow patterns was observed. The local Nu was the highest when there was no rotation of the NPO (Figure 6). At Ha = 5, CW or counter-CW rotation of the object, shifting the local peak location of Nu and reduces its value. However, on the right or left part, the local Nu attained higher values when rotations were activated because of the additional momentum of the rotations of the NPO. At Ha = 25, the secondary peaks of the local Nu were obtained and had higher values concerning rotations. However, the first peak of local Nu was significantly reduced by using the rotations of the NPO. The impacts of MaF on the local Nu at Rew = 0 and Rew = −600 are shown in Figure 7.

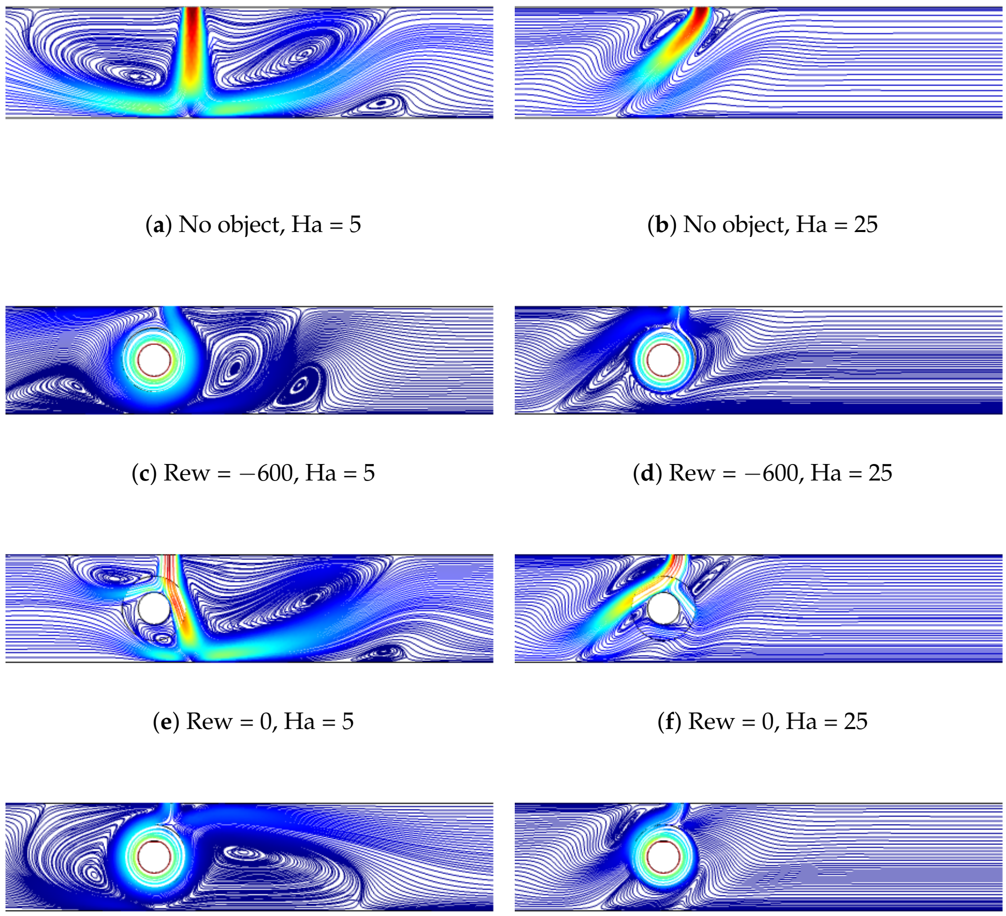

(**a**) No object, Ha = 5 (**b**) No object, Ha = 25

(**c**) Rew = −600, Ha = 5 (**d**) Rew = −600, Ha = 25

(**e**) Rew = 0, Ha = 5 (**f**) Rew = 0, Ha = 25

(**g**) Rew = 600, Ha = 5 (**h**) Rew = 600, Ha = 25

Figure 5. Effects of Rew on the streamline variations at two MaF strength levels (**c**–**h**) and configuration with no-object case (**a**,**b**) ($\mathrm{Da} = 5 \times 10^{-2}, \mathrm{Mx} = -1, \mathrm{AR} = 0.5$).

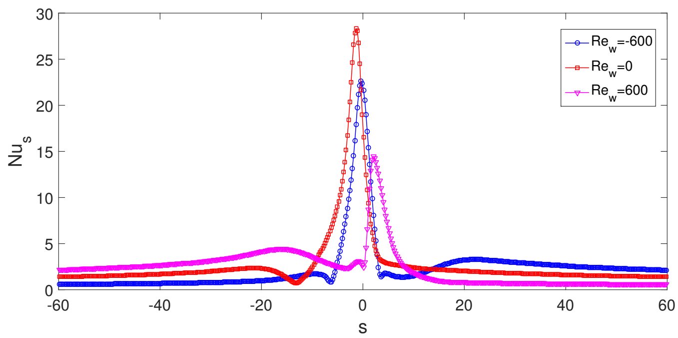

(**a**) Ha = 5

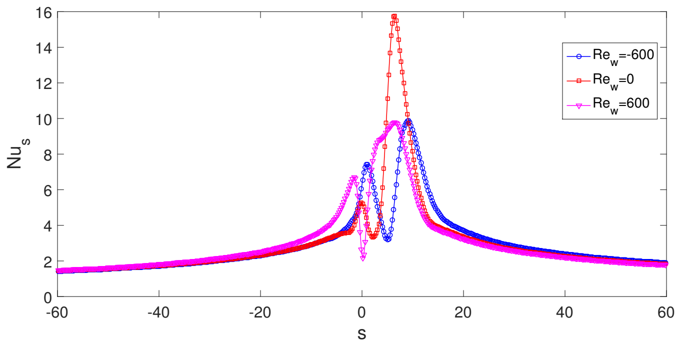

(**b**) Ha = 25

Figure 6. Local Nu variations with changes in Rew at two MaF strength levels (Da $= 5 \times 10^{-2}$, Mx $= -1$, AR $= 0.5$).

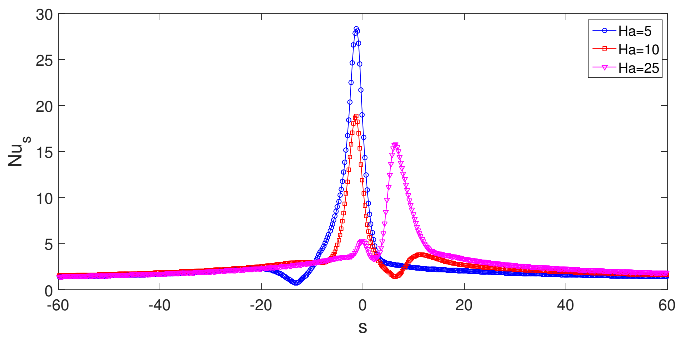

(**a**) Rew = 0

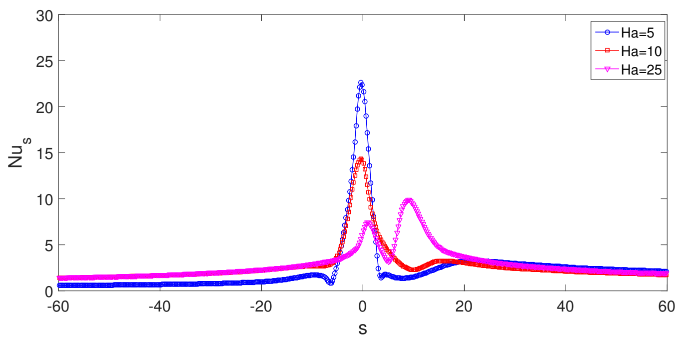

(**b**) Rew = -600

Figure 7. Impact of MaF strength on local Nu variations at two Rew (Da $= 5 \times 10^{-2}$, Mx $= -1$, AR = 0.5).

The first peak of the local Nu was reduced, but a significant increase in the second peak was observed when MaF strength was increased for both Rew = 0 and Rew = −600. When the average Nu values were considered, the presence of the rotation reduced the value by about 14.5% at Ha = 5 when lowest and highest Rew cases are compared. Less than 2% variations in the average Nu were seen when rotations were activated as compared to motionless NPO at Ha = 25. However, the local peak values were reduced by about 37% with the rotation at Ha = 25. This was due to the presence of the secondary peaks of local Nu and their significant values with the activation of rotation in both directions. When MaF strength was increased from Ha = 5 to Ha = 10, the average Nu increased for the case at Rew = −600, but the trend was the opposite for cases at Rew = 0 and without an object. For Rew = −600, this could be attributed to the suppression of the large vortex on the bottom wall. At the highest MaF strength, the average Nu attained its highest values as compared to Ha = 5, while the presence of the NPO further increased its value (Figure 8a). The highest variation in the average Nu between the cases of MaF at Ha = 5 and Ha = 25 was seen for the object with rotation at Rew = −600, which was 22%; for the case without an object, the variation was 5% (Figure 8b).

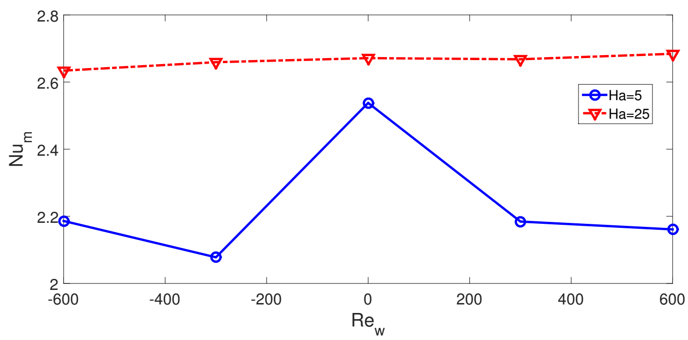

(**a**)

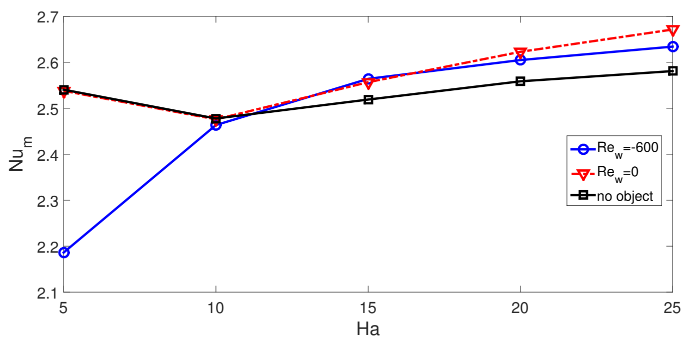

(**b**)

Figure 8. Average Nu variations with respect to changes in (**a**) Rew and (**b**) MaF strength ($\mathrm{Da} = 5 \times 10^{-2}, \mathrm{Mx} = -1, \mathrm{AR} = 0.5$).

When NPO cases with different permeability values were considered, the configuration with higher permeability at Rew = 0 resulted in a large recirculation near the inlet, while their sizes changed with lower Darcy numbers (Figure 9). The effects of the rotation of the NPO were effective for higher permeability. There was a significant reduction in the first Nu peak with a lower Darcy number for the NPO at Rew = −600 and Rew = 0. When cases with the highest and lowest permeability were compared, the first peak of Nu was reduced by about of 65% at Rew = 0 and 47% at Rew = −600 (Figure 10). The presence of rotation increased the value of the secondary peaks in the local Nu. However, the overall variation in the average Nu was less than 4% when cases of NPO with different permeability values were compared.

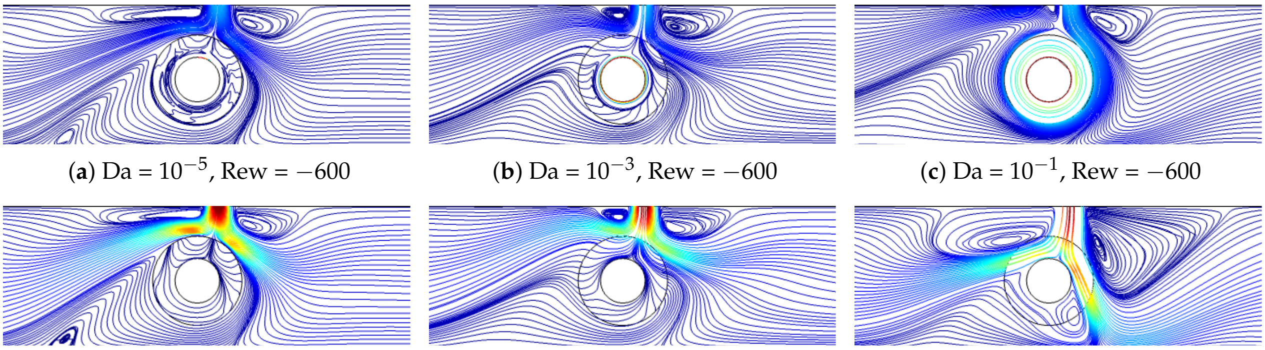

(**a**) Da = 10^{-5}, Rew = -600 (**b**) Da = 10^{-3}, Rew = -600 (**c**) Da = 10^{-1}, Rew = -600

(**d**) Da = 10^{-5}, Rew = 0 (**e**) Da = 10^{-3}, Rew = 0 (**f**) Da = 10^{-1}, Rew = 0

Figure 9. Impacts of permeability of the object on the streamline distributions at two Rew values ($\mathrm{Ha} = 10, \mathrm{Mx} = -1, \mathrm{AR} = 0.5$).

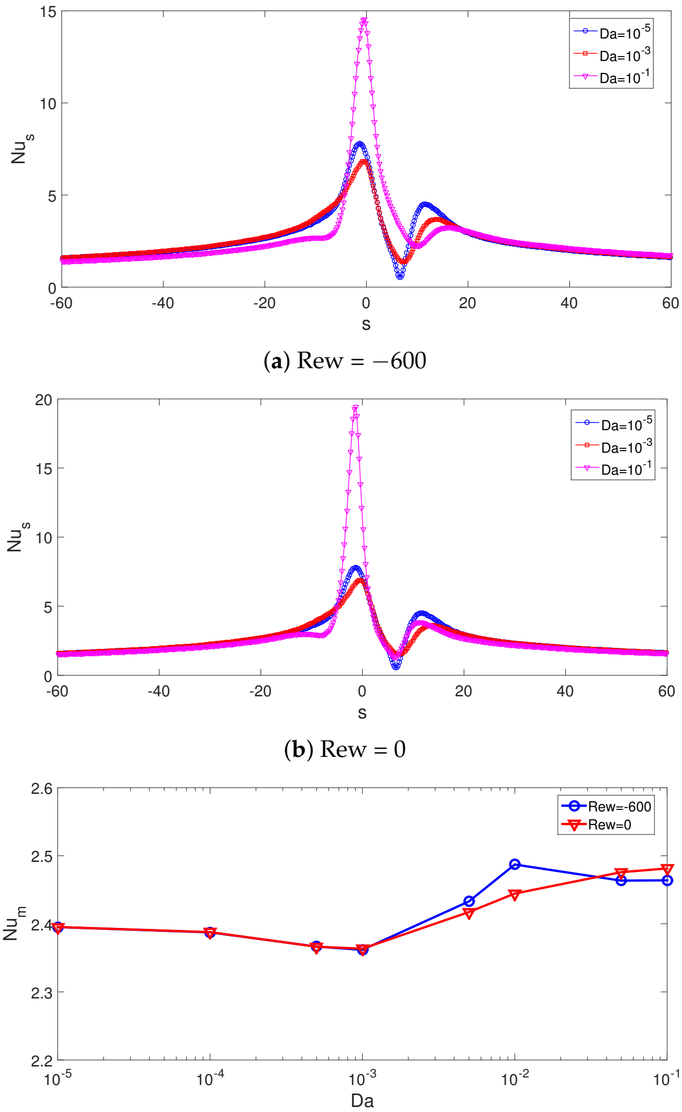

(**c**) Rew = 0

Figure 10. Effects of NPO permeability on the local and average Nu variations at two Rew values ($\mathrm{Ha} = 10, \mathrm{Mx} = -1, \mathrm{AR} = 0.5$).

The horizontal location (MX) of the NPO within the SJ-I system and its aspect ratio (AR) are other important parameters to be considered that may impact the cooling performance. Streamline distributions with varying Mx and AR at two rotational speed levels are shown in Figure 11. At Rew = 0, more deflection of the main jet stream was seen for Mx = 0, while the recirculation zone below the object was established. The vortex size above the NPO on the left side was also reduced for Mx = −2. As the rotations were activated, the vortex formations were controlled by changing the location of the NPO. At Mx = 2, due to the interaction of the main jet stream with the rotating inner surface of the object, two recirculation regions were observed in the left part of the SJ-I system. AR is defined as the ratio of the inner and outer cylinder radii of the NPO. A lower value of AR denotes a smaller rotating inner size; for higher values of AR, the impact of the rotation became effective (Figure 11g–i). At Rew = 0, when the AR increased, the vortex size near the inlet was reduced, while the small vortices established below the NPO at AR = 0.2 disappeared. When rotations with higher AR were considered, the size of the inlet vortices was reduced, while the effects of rotation on the flow field became dominant. When the NPO was located at the left side (Mx = −2), the least interaction of the porous object with main jet stream was achieved, and the local Nu peak was the highest (Figure 12). However, the highest interaction was observed at Mx = 0, while the secondary peak was lower than that with Mx = 2. The highest Nu peaks were observed at 0.122, −0.367, and 5.75 wd for the horizontal NPO locations of Mx = −2, 0, and 2, respectively. Variations in the first peak Nu were 47.8% and 15.4% when Mx = −2 and Mx = 2 were compared with Mx = 0. The higher aspect ratio of the NPO resulted in a reduction in the local Nu peak at Rew = −600 (Figure 12b), where the main cold jet stream was affected more. The average Nu attained its lowest values at Mx = −1 and Mx = 0 for stationary or rotating NPO because of the higher interaction of the jet stream with the porous cylinder and its redirection of the cold stream toward the hot surface. However, higher values were obtained when the NPO was located at Mx = −2 and Mx = 2. The highest variations in the average Nu were 8.9% at Rew = −600 and 7.5% at Rew = 0. The average Nu was generally reduced with a higher aspect ratio of the NPO. Variations in the average Nu were 9.5% and 8.5% at Rew = 0 and Rew = −600, respectively, when cases of NPO with lowest and highest AR were compared (Figure 13).

The NPO parameters on the HT were very complicated and dependent upon MaF strength, which is due to the complex interaction between the forced flow and Lorentz forces due to the inclined MaF and additional effects due to the rotation of the inner porous object's surface. Therefore, optimization studies are needed to find the optimal parameters of interest for the best cooling performance at different operating points. The COBYLA optimization algorithm was used to find the best parameters of interest, namely, the permeability, rotational speed, aspect ratio, and horizontal location of the NPO. Optimization studies were performed for each case at MaF strengths of Ha = 5, 10, and 25. The lower and upper bounds of the parameters are given in Equation (13), and the maximal average Nu was considered to be the objective function. Figure 14 shows the search for the maximal average Nu with different parameters at Ha = 5 and Ha = 25. The optimal set of parameters (Rew, Da, Mx, AR) is given in Table 2 for each case for different MaF strength levels. The corresponding Nu with the optimized configuration and without NPO is also given in the same table. The optimal parameters were different for each configuration with different MaF strength levels. A lower aspect ratio of the NPO achieved better HT performance at Ha = 10 and Ha = 25. Significant variations in the rotational speeds of the NPO were obtained to achieve better cooling performance when different MaF strength levels were considered.

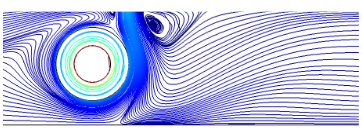
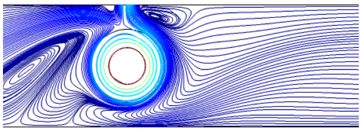
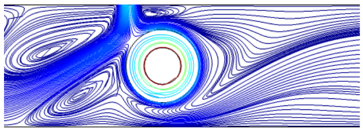

(**a**) Mx = −2, Rew = −600 (**b**) Mx = 0, Rew = −600 (**c**) Mx = 2, Rew = −600

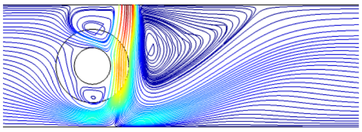
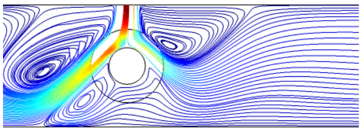
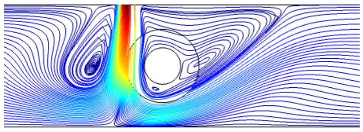

(**d**) Mx = −2, Rew = 0 (**e**) Mx = 0, Rew = 0 (**f**) Mx = 2, Rew = 0

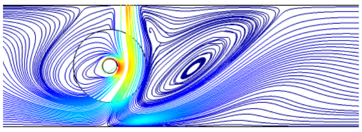
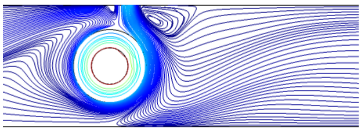
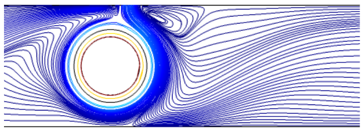

(**g**) AR = 0.2, Rew = −600 (**h**) AR = 0.5, Rew = −600 (**i**) AR = 0.8, Rew = −600

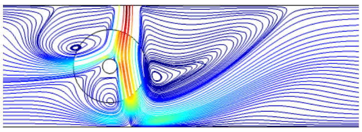
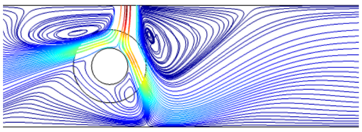
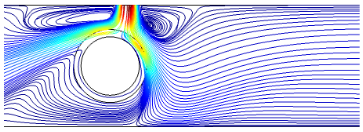

(**j**) AR = 0.2, Rew = 0 (**k**) AR = 0.5, Rew = 0 (**l**) AR = 0.8, Rew = 0

Figure 11. Effects of the location (AR = 0.5, **a**–**f**) and aspect ratio (Mx = −1, **g**–**l**) of the porous object on the variation in streamlines at two Rew values ($\mathrm{Ha} = 10, \mathrm{Da} = 5 \times 10^{-2}$).

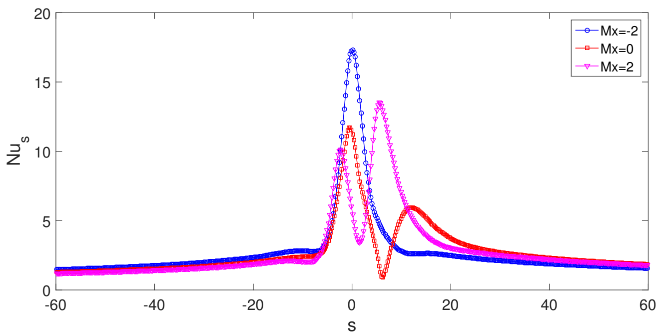

(**a**) Rew = 0

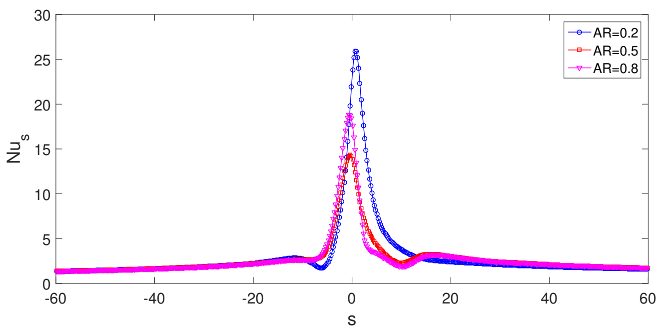

(**b**) Rew = −600

Figure 12. Local Nu distribution with varying (**a**) horizontal location and (**b**) aspect ratio of the porous object ($\mathrm{Ha} = 10, \mathrm{Da} = 5 \times 10^{-2}$).

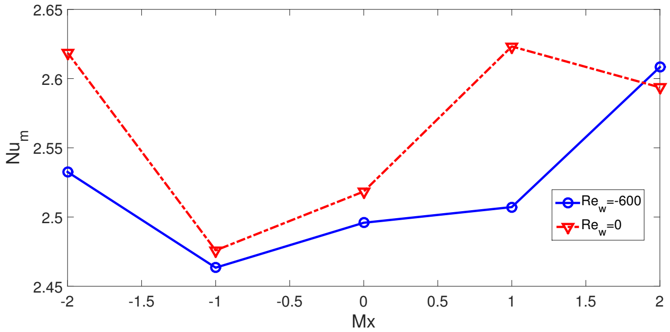

(**a**) Rew = 0

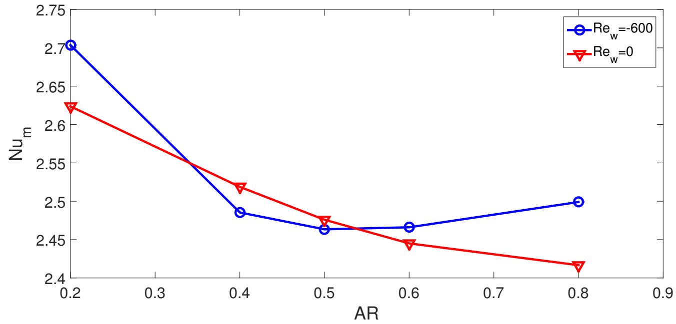

(**b**) Rew = −600

Figure 13. Average Nu versus (**a**) location and (**b**) aspect ratio of the porous object (Ha = 10, Da = 5×10^{-2}).

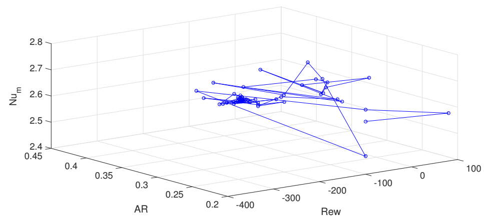

(**a**) Ha = 5

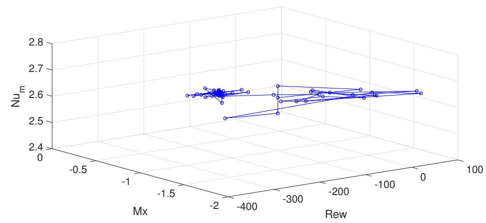

(**b**) Ha = 5

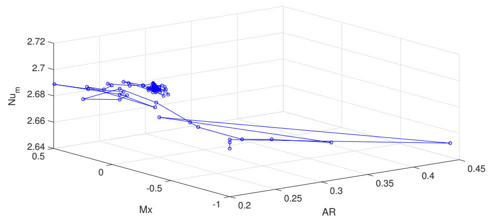

(**c**) Ha = 25

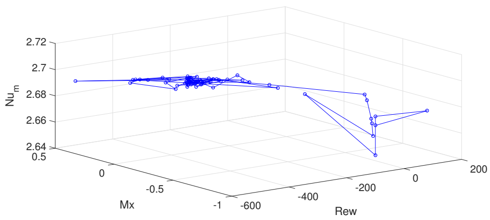

(**d**) Ha = 25

Figure 14. Search forthe maximal average Nu with the optimization solver at (**a**,**b**) Ha = 5 and (**c**,**d**) Ha = 25.

Table 2. Optimal set of parameters for the maximal average Nu at different MaF strength levels and corresponding average Nu values.

Parameter Name	At Ha = 5	At Ha = 10	At Ha = 25
Rew	−315.97	−181.167	−483.13
Da	0.0188	0.0167	0.0210
Mx	−1.456	−1.441	−0.348
AR	0.235	0.2	0.2
Average Nu	At Ha = 5	At Ha = 10	At Ha = 25
Optimum	2.74	2.67	2.71
No object	2.54	2.47	2.58

The flow-field variations at optimal conditions are shown in Figure 15, and comparisons are given for the case with parametric variation for different Ha at (Da $= 5 \times 10^{-2}$, Mx $= -1$, AR $= 0.5$). As the MaF strength increased, the suppression of the recirculation zones and the inclination of the vortices were observed for the optimized cases. The configurations were closer to the case without NPO, while the local Nu values were higher, as shown in Figure 16. Variations in the local peak between the optimized and no-object cases were 19.46%, 44.86%, and −0.54% at Ha = 5, 10, and 25, respectively, while the average Nu enhancements with the optimized NPOD device were 7.87%, 8.09%, and 5.04%. The HT enhancements (Enh) in percentages were obtained by using the average Nu results with the optimized NPO, and by using the results from parametric variations.

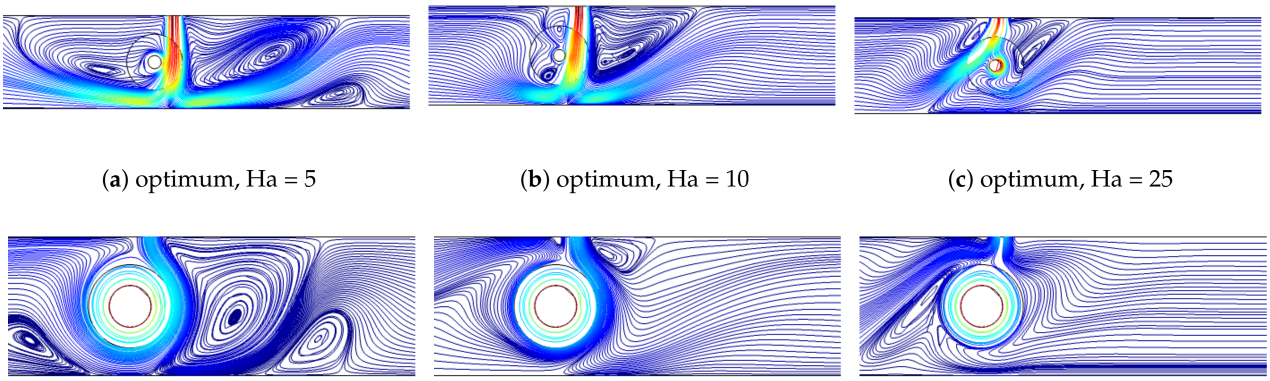

(**a**) optimum, Ha = 5 (**b**) optimum, Ha = 10 (**c**) optimum, Ha = 25

(**d**) Ha = 5, Rew = −600 (**e**) Ha = 10, Rew = −600 (**f**) Ha = 25, Rew = −600

Figure 15. Streamline variations at optimal flow conditions (**a**–**c**) and with varying MaF strength at fixed values of (Da $= 5 \times 10^{-2}$, Mx $= -1$, AR $= 0.5$).

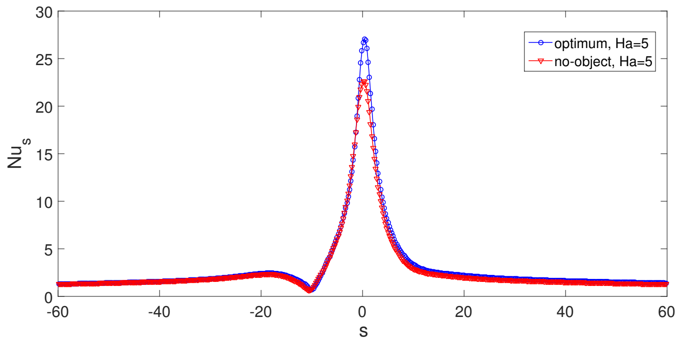

(**a**) Ha = 5

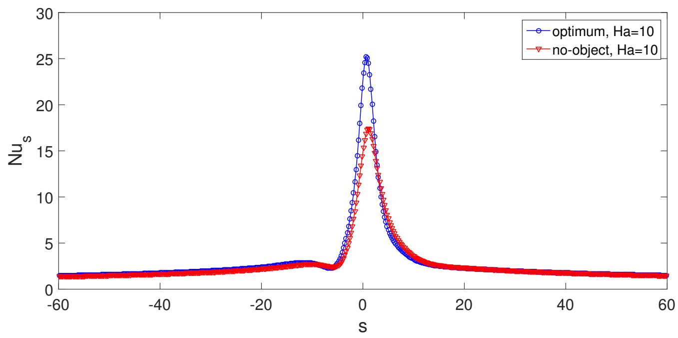

(**b**) Ha = 10

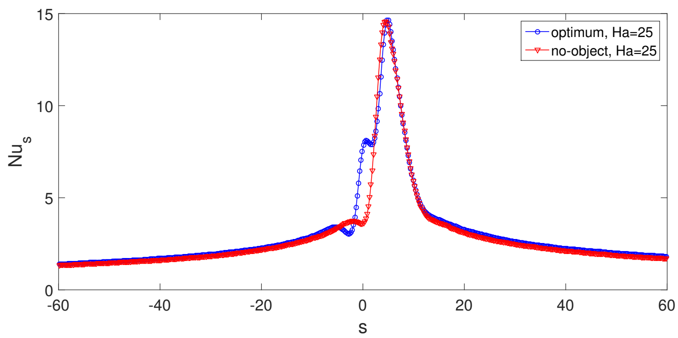

(**c**) Ha = 25

Figure 16. Comparison of local Nu variations at optimal flow conditions and in the no-object case ($\mathrm{Da} = 5 \times 10^{-2}$) considering three different MaF strength levels.

Figure 17 shows the Enh variation with respect to changes in Rew, Mx, and AR at two different MaF strength levels. The highest Enh value was 31.86% at Rew = −300 for the case of Ha = 5 when variations in Rew were compared, while this was less than 3% for the case of Ha = 25. When variations in the horizontal NPO were compared, the Enh values were higher with Ha = 5, while the maximal value was −0.54% at Mx = −1. When aspect ratio variations were compared, the highest value of Enh was 44.86% at AR = 0.8 for the configuration with Ha = 25. These results show that, by using a NPO device, excellent control for Nu variations was achieved by varying the rotational speed of the inner surface, aspect ratio, and horizontal of the device in the SJ-I system. However, further optimization is needed and should be considered to achieve the best cooling performance, which depends upon the external magnetic field's strength.

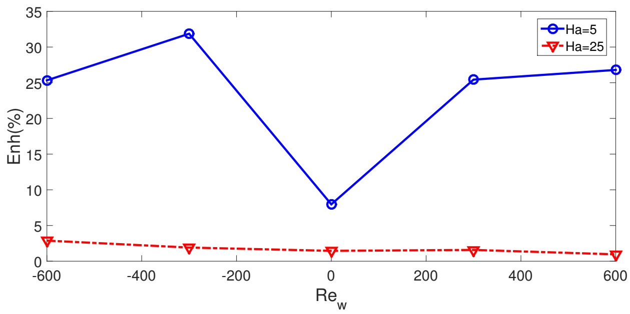

(**a**) Da $= 5 \times 10^{-2}$, Mx = -1, AR = 0.5

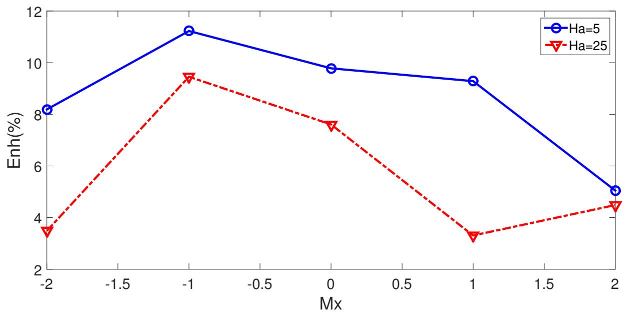

(**b**) Rew = -600, Da $= 5 \times 10^{-2}$, AR = 0.5

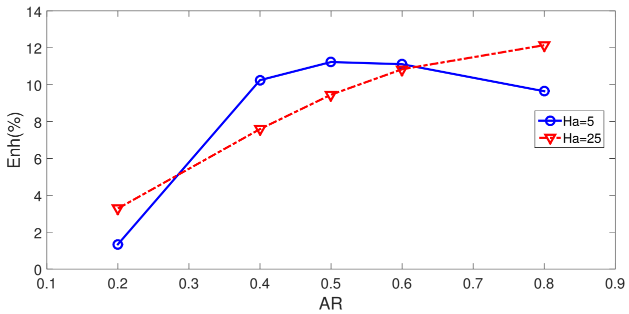

(**c**) Rew = -600, Da $= 5 \times 10^{-2}$, Mx = -1

Figure 17. Effects of (**a**) Rew, (**b**) location, and (**c**) aspect ratio of the porous object on the enhancements in the average Nu as compared to optimized flow configurations at two different MaF strength levels.

6. Conclusions

In this study, a novel porous object (NPO) was used for the flow and HT control of SJ-I cooling systems under MaF effects. The NPO was a porous annular cylinder with an inner rotating surface. A hybrid nanofluid was considered with available experimental data for effective nanofluid viscosity and thermal conductivity. The COBYLA optimization algorithm was used with CFD to find the best working parameters of the NPO at different magnetic field strengths. The presence of the object and its varying permeability, inner rotational speed, and horizontal location within the SJ-I system affect the flow and thermal field variations. As the MaF strength increased, recirculation zones were suppressed. Regarding parametric CFD, there was 14.5% variation in the average Nu at the highest rotational speed of the inner part of NPO when compared to the motionless case at Ha = 5, while it was less than 2% at Ha = 25. MaF effects were noticeable when the NPO was rotating at Rew = -600 while there was 22% variation in the average Nu for the cases between Ha = 5 and Ha = 25 at this rotational speed. The local peak of Nu varied by 47.8% when the horizontal location of the NPO was changed from Mx = 0 to Mx = -2 at Rew = -600, while the average Nu variation was 8.9%. When the lowest and highest aspect ratios of the annular NPO were considered, the average Nu variation was 9.5% at Rew = 0. Optimization-based CFD was used with the COBYLA algorithm to find the optimal set of parameters for NPO to achieve the best cooling performance at different MaF strengths. The optimal sets of (Rew, Da, Mx, AR) for NPO were (−315.97, 0.0188, −1.456, 0.235), (−181.167, 0.0167, −0.1.441, 0.2), and (−483.13, 0.0210, −0.348, 0.2) at Ha = 5, 10, and 25, respectively. When NPO was used at the optimal set of parameters, 19.46%, 44.86%, and −0.54% increments in the local Nu were achieved when compared to a no-object configuration of an SJ-I cooling system. The values were 7.87%, 8.09%, and 5.04% when the average Nu values were compared. When parametric CFD values were compared with the optimal case, different enhancements were achieved with the varying rotational speed, aspect ratio, and location of the object, and the values depended upon the strength of the MaF. Even though the NPO could be utilized as an excellent tool for convective HT control, the best performance of the system and the efficient utilization of the object can be achieved by using optimization-assisted CFD rather than parametric CFD.

Author Contributions: Conceptualization, F.S.; methodology, F.S., L.K. and B.A.; software, F.S.; validation, L.K.; formal analysis, F.S., W.A. and L.K.; investigation, F.S., L.K., W.A., L.B.S. and B.M.A.; writing—original draft preparation, F.S.; writing—review and editing, F.S., B.A., L.K., W.A., S.A.B. and L.K.; visualization, F.S. and L.K.; supervision, F.S., B.A., L.K., W.A., S.A.B., H.G. and L.B.S. All authors have read and agreed to the published version of the manuscript.

Funding: This research was funded by Scientific Research Deanship at University of Ha'il–Saudi Arabia through project number RG-21 057.

Institutional Review Board Statement: Not applicable.

Informed Consent Statement: Not applicable.

Data Availability Statement: Not applicable.

Conflicts of Interest: The authors declare no conflict of interest.

Abbreviations

The following abbreviations are used in this manuscript:

AR	Aspect ratio
Da	Darcy number
Dh	Hydraulic diameter, (m)
F	Nodal value
h	Heat transfer coefficient, (W/m^{2}K)
H	Separating distance, (m)
Ha	Hartmann number
k	Thermal conductivity, (W/mK)
L	Plate length, (m)
Mx	Dimensionless horizontal distance
n	Unit normal vector
Nu	Nusselt number
p	Pressure, (Pa)
Pr	Prandtl number
R	Residual
Re	Reynolds number
Rew	Rotational Reynolds number
T	Temperature, (K)
u, *v*	x–y velocity components, (m/s)
Vr	Field variable
W	Weight function
wd	Slot width, (m)
x, *y*	Cartesian coordinates, (m)

Greek Characters	
α	Thermal diffusivity, (m^2/s)
θ	Nondimensional temperature
μ	Dynamic viscosity, (Pa.s)
ν	Kinematic viscosity, (m^2/s)
ρ	Density of the fluid, (kg/m^3)
ω	Rotational velocity, (rad/s)
ε	Porosity
κ	Permeability, (m^2)
σ	Electrical conductivity, (S/m)
Φ^s	Shape function
Subscripts	
c	Cold wall
h	Hot wall
m	Average
nf	Nanofluid
Abbreviations	
CFD	Computational fluid dynamics
COBYLA	constrained optimization by linear approximations
FEM	Finite element method
HT	Heat transfer
MF	Magnetic field
NPO	Novel porous object
SJ-I	Slot jet impingement

References

1. Jambunathan, K.; Lai, E.; Moss, M.; Button, B. A review of heat transfer data for single circular jet impingement. *Int. J. Heat Fluid Flow* **1992**, *13*, 106–115. [CrossRef]
2. Krishan, G.; Aw, K.C.; Sharma, R.N. Synthetic jet impingement heat transfer enhancement—A review. *Appl. Therm. Eng.* **2019**, *149*, 1305–1323. [CrossRef]
3. Liewkongsataporn, W.; Patterson, T.; Ahrens, F. Pulsating jet impingement heat transfer enhancement. *Dry. Technol.* **2008**, *26*, 433–442. [CrossRef]
4. Li, P.; Guo, D.; Liu, R. Mechanism analysis of heat transfer and flow structure of periodic pulsating nanofluids slot-jet impingement with different waveforms. *Appl. Therm. Eng.* **2019**, *152*, 937–945. [CrossRef]
5. Abishek, S.; Narayanaswamy, R. Low frequency pulsating jet impingement boiling and single phase heat transfer. *Int. J. Heat Mass Transf.* **2020**, *159*, 120052. [CrossRef]
6. Gau, C.; Chung, C. Surface curvature effect on slot-air-jet impingement cooling flow and heat transfer process. *J. Heat Transfer.* **1991**, *113*, 858–864. [CrossRef]
7. Zhou, Y.; Lin, G.; Bu, X.; Bai, L.; Wen, D. Experimental study of curvature effects on jet impingement heat transfer on concave surfaces. *Chin. J. Aeronaut.* **2017**, *30*, 586–594. [CrossRef]
8. Selimefendigil, F.; Öztop, H.F. Al_2O_3-water nanofluid jet impingement cooling with magnetic field. *Heat Transf. Eng.* **2020**, *41*, 50–64. [CrossRef]
9. Wong, K.C.; Saeid, N.H. Numerical study of mixed convection on jet impingement cooling in a horizontal porous layer under local thermal non-equilibrium conditions. *Int. J. Therm. Sci.* **2009**, *48*, 860–870. [CrossRef]
10. Lam, P.A.K.; Prakash, K.A. A numerical investigation of heat transfer and entropy generation during jet impingement cooling of protruding heat sources without and with porous medium. *Energy Convers. Manag.* **2015**, *89*, 626–643. [CrossRef]
11. Sivasamy, A.; Selladurai, V.; Kanna, P.R. Mixed convection on jet impingement cooling of a constant heat flux horizontal porous layer. *Int. J. Therm. Sci.* **2010**, *49*, 1238–1246. [CrossRef]
12. Koriko, O.; Adegbie, K.; Oke, A.; Animasaun, I. Exploration of Coriolis force on motion of air over the upper horizontal surface of a paraboloid of revolution. *Phys. Scr.* **2020**, *95*, 035210. [CrossRef]
13. Oke, A.; Animasaun, I.; Mutuku, W.; Kimathi, M.; Shah, N.A.; Saleem, S. Significance of Coriolis force, volume fraction, and heat source/sink on the dynamics of water conveying 47 nm alumina nanoparticles over a uniform surface. *Chin. J. Phys.* **2021**, *71*, 716–727. [CrossRef]
14. Yacob, N.A.; Dzulkifli, N.F.; Salleh, S.N.A.; Ishak, A.; Pop, I. Rotating flow in a nanofluid with CNT nanoparticles over a stretching/shrinking surface. *Mathematics* **2021**, *10*, 7. [CrossRef]
15. Roslan, R.; Saleh, H.; Hashim, I. Effect of rotating cylinder on heat transfer in a square enclosure filled with nanofluids. *Int. J. Heat Mass Transf.* **2012**, *55*, 7247–7256. [CrossRef]

16. Khedher, N.B.; Selimefendigil, F.; Kolsi, L.; Aich, W.; Ben Said, L.; Boukholda, I. Performance Optimization of a Thermoelectric Device by Using a Shear Thinning Nanofluid and Rotating Cylinder in a Cavity with Ventilation Ports. *Mathematics* **2022**, *10*, 1075. [CrossRef]
17. Hassen, W.; Selimefendigil, F.; Ben Khedher, N.; Kolsi, L.; Borjini, M.N.; Alresheedi, F. Control of magnetohydrodynamic mixed convection and entropy generation in a porous cavity by using double rotating cylinders and curved partition. *ACS Omega* **2021**, *6*, 35607–35618. [CrossRef]
18. Wang, L.; Sundén, B.; Borg, A.; Abrahamsson, H. Control of jet impingement heat transfer in crossflow by using a rib. *Int. J. Heat Mass Transf.* **2011**, *54*, 4157–4166. [CrossRef]
19. Iwana, T.; Suenaga, K.; Shirai, K.; Kameya, Y.; Motosuke, M.; Honami, S. Heat transfer and fluid flow characteristics of impinging jet using combined device with triangular tabs and synthetic jets. *Exp. Therm. Fluid Sci.* **2015**, *68*, 322–329. [CrossRef]
20. Selimefendigil, F.; Öztop, H.F. Cooling of a partially elastic isothermal surface by nanofluids jet impingement. *J. Heat Transf.* **2018**, *140*, 042205. [CrossRef]
21. Nagesha, K.; Srinivasan, K.; Sundararajan, T. Enhancement of jet impingement heat transfer using surface roughness elements at different heat inputs. *Exp. Therm. Fluid Sci.* **2020**, *112*, 109995. [CrossRef]
22. Díaz, J.L.; Rahman, S.; García-Haro, J.M. Heterogeneous Diffusion, Stability Analysis, and Solution Profiles for a MHD Darcy—Forchheimer Model. *Mathematics* **2021**, *10*, 20. [CrossRef]
23. Oke, A.S. Heat and Mass Transfer in 3D MHD Flow of EG-Based Ternary Hybrid Nanofluid Over a Rotating Surface. *Arab. J. Sci. Eng.* **2022**, 1–17. [CrossRef]
24. Selimefendigil, F.; Öztop, H.F. MHD Pulsating forced convection of nanofluid over parallel plates with blocks in a channel. *Int. J. Mech. Sci.* **2019**, *157*, 726–740. [CrossRef]
25. Chamkha, A.J.; Selimefendigil, F.; Oztop, H.F. Effects of a rotating cone on the mixed convection in a double lid-driven 3D porous trapezoidal nanofluid filled cavity under the impact of magnetic field. *Nanomaterials* **2020**, *10*, 449. [CrossRef]
26. Ghachem, K.; Selimefendigil, F.; Öztop, H.F.; Alhadri, M.; Kolsi, L.; Alshammari, N. Impacts of rotating surface and area expansion during nanofluid convection on phase change dynamics for PCM packed bed installed cylinder. *Alex. Eng. J.* **2022**, *61*, 4159–4173. [CrossRef]
27. Oke, A. Coriolis effects on MHD flow of MEP fluid over a non-uniform surface in the presence of thermal radiation. *Int. Commun. Heat Mass Transf.* **2021**, *129*, 105695. [CrossRef]
28. Selimefendigil, F.; Öztop, H.F. Hydro-thermal performance of CNT nanofluid in double backward facing step with rotating tube bundle under magnetic field. *Int. J. Mech. Sci.* **2020**, *185*, 105876. [CrossRef]
29. M'hamed, B.; Sidik, N.A.C.; Yazid, M.N.A.W.M.; Mamat, R.; Najafi, G.; Kefayati, G. A review on why researchers apply external magnetic field on nanofluids. *Int. Commun. Heat Mass Transf.* **2016**, *78*, 60–67. [CrossRef]
30. Sheikholeslami, M.; Rokni, H.B. Magnetohydrodynamic CuO–water nanofluid in a porous complex-shaped enclosure. *J. Therm. Sci. Eng. Appl.* **2017**, *9*, 041007. [CrossRef]
31. Li, Q.; Xuan, Y.; Yu, F. Experimental investigation of submerged single jet impingement using Cu-water nanofluid. *Appl. Therm. Eng.* **2012**, *36*, 426–433. [CrossRef]
32. Nguyen, C.T.; Galanis, N.; Polidori, G.; Fohanno, S.; Popa, C.V.; Beche, A.L. An experimental study of a confined and submerged impinging jet heat transfer using Al_2O_3-water nanofluid. *Int. J. Therm. Sci.* **2009**, *48*, 401–411. [CrossRef]
33. Selimefendigil, F.; Oztop, H.F. Pulsating nanofluids jet impingement cooling of a heated horizontal surface. *Int. J. Heat Mass Transf.* **2014**, *69*, 54–65. [CrossRef]
34. Mohammadpour, J.; Lee, A. Investigation of nanoparticle effects on jet impingement heat transfer: A review. *J. Mol. Liq.* **2020**, *316*, 113819. [CrossRef]
35. Tyagi, P.K.; Kumar, R.; Mondal, P.K. A review of the state-of-the-art nanofluid spray and jet impingement cooling. *Phys. Fluids* **2020**, *32*, 121301. [CrossRef]
36. Lee, H.; Ha, M.; Yoon, H. A numerical study on the fluid flow and heat transfer in the confined jet flow in the presence of magnetic field. *Int. J. Heat Mass Transf.* **2005**, *48*, 5297–5309. [CrossRef]
37. Nimmagadda, R.; Haustein, H.D.; Asirvatham, L.G.; Wongwises, S. Effect of uniform/non-uniform magnetic field and jet impingement on the hydrodynamic and heat transfer performance of nanofluids. *J. Magn. Magn. Mater.* **2019**, *479*, 268–281. [CrossRef]
38. Selimefendigil, F.; Öztop, H.F. Performance assessment of a thermoelectric module by using rotating circular cylinders and nanofluids in the channel flow for renewable energy applications. *J. Clean. Prod.* **2021**, *279*, 123426. [CrossRef]
39. Sheremet, M.A.; Oztop, H.; Pop, I.; Al-Salem, K. MHD free convection in a wavy open porous tall cavity filled with nanofluids under an effect of corner heater. *Int. J. Heat Mass Transf.* **2016**, *103*, 955–964. [CrossRef]
40. Mehrez, Z.; Cafsi, A.E.; Belghith, A.; Quere, P.L. MHD effects on heat transfer and entropy generation of nanofluid flow in an open cavity. *J. Magn. Magn. Mater.* **2015**, *374*, 214–224. [CrossRef]
41. Powell, M.J. A direct search optimization method that models the objective and constraint functions by linear interpolation. In *Advances in Optimization and Numerical Analysis*; Springer: Dodrecht, The Netherlands, 1994; Volume 275, pp. 51–67.
42. Silva, S.R.; Gomes, R.; Falcao, A. Hydrodynamic optimization of the UGEN: Wave energy converter with U-shaped interior oscillating water column. *Int. J. Mar. Energy* **2016**, *15*, 112–126. [CrossRef]

43. Sheikholeslami, M.; Shamlooei, M. Convective flow of nanofluid inside a lid driven porous cavity using CVFEM. *Phys. B Condens. Matter* **2017**, *521*, 239–250. [CrossRef]
44. Chiriac, V.A.; Ortega, A. A numerical study of the unsteady flow and heat transfer in a transitional confined slot jet impinging on an isothermal surface. *Int. J. Heat Mass Transf.* **2002**, *45*, 1237–1248. [CrossRef]
45. Chou, Y.; Hung, Y. Impingement cooling of an isothermally heated surface with a confined slot jet. *ASME Trans. J. Heat Transf.* **1994**, *116*, 479–482. [CrossRef]
46. Manca, O.; Ricci, D.; Nardini, S.; Di Lorenzo, G. Thermal and fluid dynamic behaviors of confined laminar impinging slot jets with nanofluids. *Int. Commun. Heat Mass Transf.* **2016**, *70*, 15–26. [CrossRef]